



# Acoustic force spectroscopy reveals subtle differences in cellulose unbinding behavior of carbohydrate-binding modules

Markus Hackl<sup>a</sup>, Edward V. Contrada<sup>a</sup>, Jonathan E. Ash<sup>a</sup>, Atharv Kulkarni<sup>a</sup>, Jinho Yoon<sup>b</sup>, Hyeon-Yeol Cho<sup>b</sup>, Ki-Bum Lee<sup>b</sup>, John M. Yarbrough<sup>c</sup>, Cesar A. López<sup>d</sup>, Sandrasegaram Gnanakaran<sup>d</sup>, and Shishir P. S. Chundawat<sup>a,1</sup>

Edited by Alexis Bell, University of California, Berkeley, CA; received September 22, 2021; accepted August 25, 2022

Protein adsorption to solid carbohydrate interfaces is critical to many biological processes, particularly in biomass deconstruction. To engineer more-efficient enzymes for biomass deconstruction into sugars, it is necessary to characterize the complex protein–carbohydrate interfacial interactions. A carbohydrate-binding module (CBM) is often associated with microbial surface-tethered cellulosomes or secreted cellulase enzymes to enhance substrate accessibility. However, it is not well known how CBMs recognize, bind, and dissociate from polysaccharides to facilitate efficient cellulolytic activity, due to the lack of mechanistic understanding and a suitable toolkit to study CBM–substrate interactions. Our work outlines a general approach to study the unbinding behavior of CBMs from polysaccharide surfaces using a highly multiplexed single-molecule force spectroscopy assay. Here, we apply acoustic force spectroscopy (AFS) to probe a *Clostridium thermocellum* cellulosomal scaffolding protein (CBM3a) and measure its dissociation from nanocellulose surfaces at physiologically relevant, low force loading rates. An automated microfluidic setup and method for uniform deposition of insoluble polysaccharides on the AFS chip surfaces are demonstrated. The rupture forces of wild-type CBM3a, and its Y67A mutant, unbinding from nanocellulose surfaces suggests distinct multimodal CBM binding conformations, with structural mechanisms further explored using molecular dynamics simulations. Applying classical dynamic force spectroscopy theory, the single-molecule unbinding rate at zero force is extrapolated and found to agree with bulk equilibrium unbinding rates estimated independently using quartz crystal microbalance with dissipation monitoring. However, our results also highlight critical limitations of applying classical theory to explain the highly multivalent binding interactions for cellulose–CBM bond rupture forces exceeding 15 pN.

carbohydrate-binding module | nanocellulose | single-molecule force spectroscopy | acoustic force spectroscopy | biofuels

Carbohydrate-based biopolymers are abundant throughout all forms of life and play a major part in biomolecular recognition processes that have fundamental scientific and applied technological relevance. Protein adsorption to simple or complex carbohydrates at solid interfaces is a critical step in biological processes such as plant growth (1, 2), host infection (3–5), or biofuels production (6, 7). Although carbohydrates display structural diversity, many carbohydrate-binding modules (CBMs) that bind to diverse carbohydrates often display a structurally similar binding site architecture (8). Therefore, insight into a particular CBM–carbohydrate system would help unravel general principles of protein–carbohydrate binding. Carbohydrate-active enzymes (CAZymes) are a well-studied domain and suitable model system to further investigate molecular-level interactions. CAZymes, such as processive cellulases, often consist of two or more domains called carbohydrate-binding module and catalytic domain (CD), which are responsible for the recognition/binding and breakdown of the substrate, respectively (9). On the other hand, cellulosomes are larger multidomain enzymes where CDs are assembled on a scaffolding domain decorated with CBMs and specific linker domains as shown in Fig. 1A (10). Cellulosomes adapt to the substrate topology and display a “sit-and-dig” mechanism where the cellulosome degrades individual cellulose crystals without dissociating from the substrate (11–13). This mode of action contrasts processive cellulases, such as *Trichoderma reesei* Cel7A, which displays a “slide-and-peel” mechanism and frequently dissociates from the substrate (9, 14–16).

Carbohydrate binding modules can be grouped into type A, B, or C categories based on relevant structural–functional relationships. Both *Ti*Cel7A and the cellulosome from *Clostridium thermocellum* possess a type A CBM with a similar overarching architecture of the cellulose binding site. Type A CBMs preferably bind to insoluble and highly crystalline cellulose, forming a planar flat, platform-like binding surface mostly lined with aromatic residues, complementary to the flat planar structure of the

## Significance

Cellulases are multimodular enzymes produced by microbes that catalyze cellulose hydrolysis into glucose. These enzymes play an important role in global carbon cycling as well as cellulosic biofuel production. CBMs are essential components of cellulolytic enzymes involved in facilitating the hydrolysis of polysaccharides by a tethered catalytic domain (CD). The subtle interplay between CBM binding and CD activity is poorly understood, particularly for heterogeneous reactions at solid–liquid interfaces. Here, we report a single-molecule force spectroscopy method to study CBM dissociation from cellulose to infer the molecular mechanism governing substrate recognition and dissociation. This approach can be broadly applied to study multivalent protein–polysaccharide binding interactions relevant to other carbohydrates, such as starch, chitin, or hyaluronan, to engineer efficient biocatalysts.

Author contributions: M.H., S.G., and S.P.S.C. designed research; M.H., E.V.C., J.E.A., A.K., J.Y., H.-Y.C., K.-B.L., J.M.Y., and C.A.L. performed research; M.H., E.V.C., J.E.A., and C.A.L. analyzed data; and M.H. and S.P.S.C. wrote the paper.

The authors declare no competing interest.

This article is a PNAS Direct Submission.

Copyright © 2022 the Author(s). Published by PNAS. This article is distributed under Creative Commons Attribution-NonCommercial-NoDerivatives License 4.0 (CC BY-NC-ND).

<sup>1</sup>To whom correspondence may be addressed. Email: shishir.chundawat@rutgers.edu.

This article contains supporting information online at <http://www.pnas.org/lookup/suppl/doi:10.1073/pnas.2117467119/-/DCSupplemental>.

Published October 10, 2022.

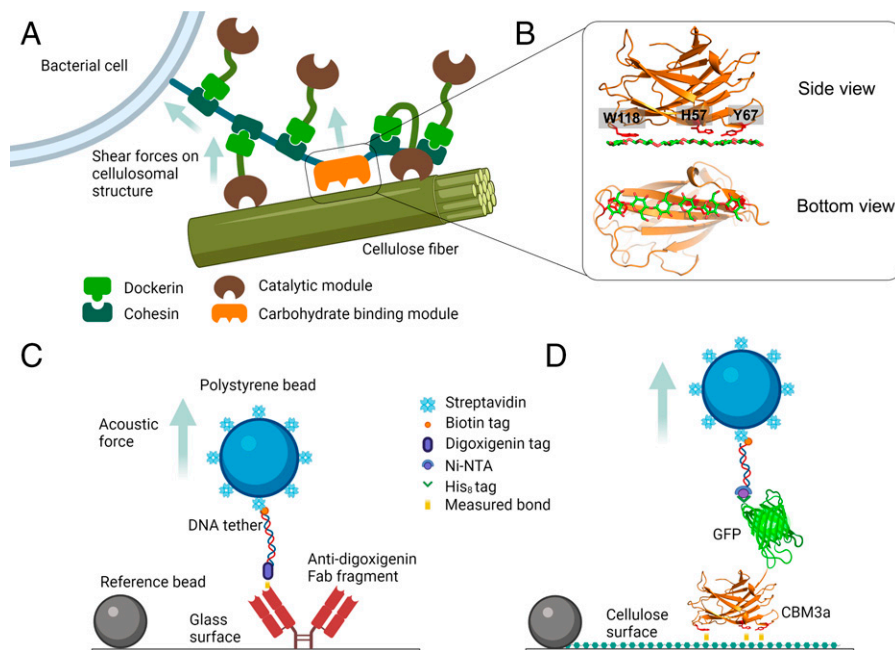


**Fig. 1.** Schematic of a generic cellulosome and AFS experimental setup to characterize single-molecule model protein–ligand and CBM3a–polysaccharide unbinding forces (not to scale). (A) Generic bacterial cell surface-anchored cellulosome is shown adhering to a single cellulose fiber. The CBM binds to cellulose and directs the CDs to the cellulose surface. Shear forces due to the substrate or cell movement are exerted on the cellulosome scaffold. (B) Side and bottom view of CBM3a structure with key aromatic residues involved in binding to cellulose (PDB ID: 1NBC). The aromatic residues W118, H57, and Y67 form a flat binding surface complementary to the cellulose surface. (C) Schematic outlining the measurement of the unbinding force of model DIG ligand from surface-bound aDIG antibody to validate the bead preparation method as well as analysis procedure of AFS traces. (D) Schematic outlining the measurement of the unbinding force of His-GFP tagged CBM3a from an NCC surface using the AFS assay.

crystalline substrate (17). As such, CBM1 from *T<sub>7</sub>Cel7A* exhibits three tyrosine residues at the 5, 31, and 32 positions (18), whereas the three aromatic residues on the binding surface of *C<sub>1</sub>*CBM3a are H57, Y67, and W118, respectively (19), as shown in Fig. 1B. Although mutations of the aromatic residues of CBM3a to alanine can reduce the apparent bulk ensemble binding affinity to native crystalline cellulose, the enzymatic activity of endocellulases fused to those mutants increased by 20 to 70% compared to the wild type (20). Altering enzyme binding affinity to cellulosic substrates is being explored as a strategy to engineer more efficient cellulases (21, 22). However, engineering highly active cellulases, cellulosomes, and associated cellulolytic microbes still presents challenges due to the inadequate understanding of the complex interplay between CD and CBM as well as the multivalent nature of the CBM–carbohydrate interactions.

Traditionally, CBM and cellulase adsorption is characterized by bulk ensemble-based methods such as solid-phase depletion (23, 24), quartz crystal microbalance with dissipation (QCM-D) (25), and isothermal titration calorimetry (26, 27). However, these methods rely on simplified models to illustrate binding interactions that do not reflect the underlying molecular mechanism of protein binding to highly multivalent carbohydrate ligands such as cellulose. Techniques like single-molecule fluorescence (16, 28) and force spectroscopy (29) have greatly contributed to our understanding of molecular processes relevant to cellulose degradation. In particular, atomic force microscopy (AFM) has been used previously to characterize CBM desorption from cellulose on the single-molecule level (30, 31). Examples include the identification of binding sites (32), distinguishing specific from nonspecific binding (33), and determining the zero-force unbinding rate using Bell's model (34). Although AFM measures force and distance with piconewton and nanometer resolution, the determination of unbinding forces occurs far from equilibrium, due to the relatively high loading rates inherent in the conventional AFM technique, potentially

obscuring multimodal unbinding behavior seen at physiologically relevant conditions. Alternatively, optical tweezers (OT) have been used to study CBM unbinding at lower loading rates and force-clamp mode (35), and the results suggest a complex unbinding behavior where the bond lifetime data do not follow a single exponential decay function unlike what was originally suggested by AFM studies (34).

In contrast to AFM, acoustic force spectroscopy (AFS) is a technique that enables the application of low loading rates comparable to OTs while maintaining a higher throughput during single-molecule force spectroscopy (SMFS) assays (36, 37). Similar to OT, the protein of interest is attached to a micrometer-sized bead via a double-stranded DNA (dsDNA) tether. However, forces on the bead are exerted by acoustic standing waves. Streptavidin-coated beads are commonly used to connect biotinylated DNA tethers (38) due to their high specificity and binding strength (39, 40). On the other end of the tether, the protein of interest is either covalently linked through a thiol–maleimide cross-link (29) or tethered noncovalently via the histidine tag to Anti-his antibodies, which, in turn, are covalently linked to aminated DNA tethers (35). The histidine tag of proteins was used previously to noncovalently link to DNA (41–44) and directly attach proteins to nitrilotriacetic acid (NTA)-modified AFM tips (45). It was demonstrated that the His–Ni–NTA bond is stable enough (~120 pN at 400 pN/s) to facilitate SMFS experiments of the tethered protein (46–49), thus allowing AFM-based studies to measure unbinding forces of CBM3a using Ni–NTA (31, 33).

Here, we combine the tethering methods by directly synthesizing a linear dsDNA tether with biotin on one end, to attach it to a micrometer-sized bead, and Ni–NTA on the other end, to tether any His-tagged protein. This setup allows SMFS of the His-tagged protein with its polysaccharide ligand deposited onto the AFS microfluidic channel surface to enable high-throughput assays. Such tethers can be used in other tethered bead setups

such as optical or magnetic tweezers, highlighting the modularity and versatility of our approach. Furthermore, digoxigenin (DIG) tethers instead of NTA were generated with the same procedure to validate the bead preparation method and analysis of the recorded position and force–distance traces using AFS. A schematic of the protein–ligand systems studied to measure bond rupture forces is shown in Fig. 1 *C* and *D*. Furthermore, an automated method for depositing nanocrystalline cellulose (NCC) inside the AFS chip was developed. The unbinding forces of *C. thermocellum* CBM3a-wt (wild type [WT]) and its Y67A mutant were measured at fixed, low loading rates. The unbinding forces of the WT have been previously characterized by AFM (31–34). Furthermore, it was shown previously that the Y67A mutation reduces CBM binding affinity by several orders of magnitude while improving tethered CD activity for reasons not clear (20). The unbinding behavior of the WT and mutant CBM3a using SMFS measured at physiologically relevant conditions has not yet been reported. We identified a clear difference in the rupture force distribution pattern observed between WT and Y67A mutant at low loading rates that are often not accessible by alternative SMFS methods like AFM. While the extracted unbinding rate ( $k_{off}$ ) from our AFS results agrees with bulk ensemble QCM-D results, the classical SMFS model is unable to accurately capture the multivalent protein–polysaccharide binding interactions, particularly at higher rupture forces. Lastly, molecular dynamics (MD) simulations were performed to provide detailed atomistic structural insights into how a single mutation in the planar binding motif of CBM3a can severely disrupt its multimodal interactions with nanocellulose that were readily probed using our AFS technique.

## Results

**Deposition and Characterization of Nanocellulose inside the AFS Chip.** Sulfuric acid–derived NCC was used to generate the cellulose model film in this study. The formation of an NCC

film inside the AFS chip was accomplished by a multilayer deposition process (50) where poly-L-Lysine (PLL) and NCC were alternately deposited using an automated microfluidic control system. Fig. 2 *A* and *B* shows the flowchart and process flow diagram of the process, and a detailed description can be found in *Materials and Methods*. Green fluorescent protein (GFP) tagged CBM3a was expressed as described previously (20) and used to visualize the cellulose film deposited on the AFS chip. Fig. 2*C* shows a representative fluorescence image of the NCC-modified AFS chip labeled with GFP-CBM3a. The arrow indicates an area where a bubble was stuck during the NCC deposition process. Slightly lower amounts of NCC were deposited in that area, resulting in lower fluorescence. The rest of the flow channel displays a uniform fluorescence, indicating that NCC is deposited evenly across the channel. The average fluorescence intensity of the bare glass and PLL-treated chips surfaces is  $14 \pm 1$  a.u. (mean  $\pm$  SEM) and  $12 \pm 3$  a.u., respectively, whereas the NCC-treated chips show a fluorescence intensity of  $136 \pm 35$  a.u. The deposition of a single layer of NCC onto a PLL-treated surface resulted in a fluorescence intensity of  $42 \pm 24$  a.u. Despite significantly higher fluorescence compared to controls, such prepared AFS chips failed to reproducibly provide a consistent response at the single-molecule level, even though AFM imaging confirmed the deposition of a uniform layer of NCC (*SI Appendix, Fig. S1*). A relationship between the success of a single-molecule experiment and the measured fluorescence intensity was observed, where the likelihood of a successful single-molecule experiment positively correlated with the measured fluorescence. Hence, a multilayer NCC deposition method was used to ensure a consistently high fluorescence signal, which, in turn, resulted in a reliable rupture force measurement of CBMs. Multilayer NCC-functionalized AFS chips, which were subsequently cleaned and imaged as outlined in *Materials and Methods*, showed a fluorescence intensity of  $13 \pm 0.5$ , indicating the removal of NCC for reuse of the AFS chips for multiple rounds of experimentation. Fig. 2*D* shows an example surface

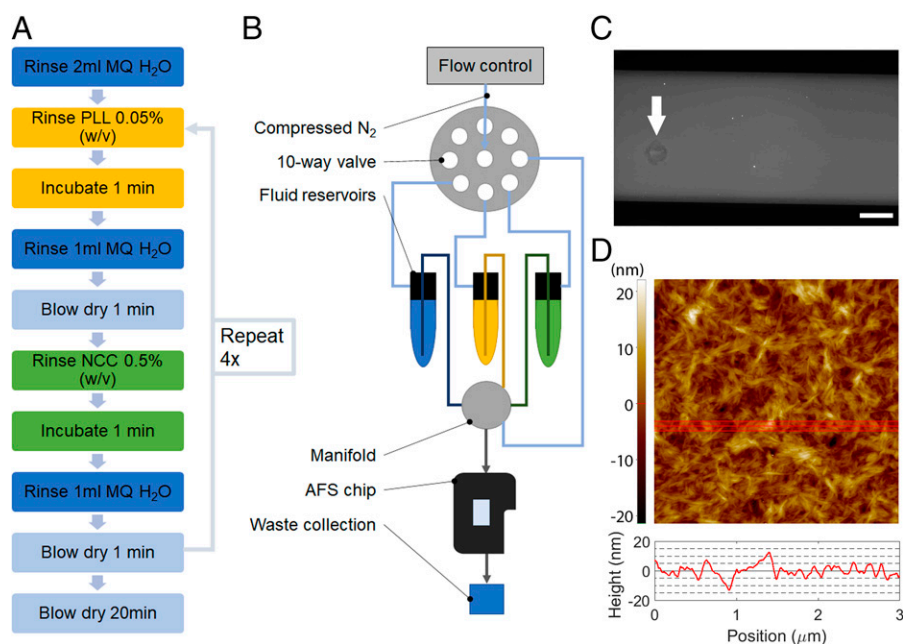


**Fig. 2.** Multilayer deposition of NCC within the AFS chip enables the characterization of a uniform and reproducible surface. (A) Flowchart and (B) process flow diagram of the NCC deposition method, (C) Fluorescence image of the NCC-modified AFS chip. GFP-CBM3a-wt was used to bind to and visualize the deposited NCC film. The arrow indicates a representative area where a bubble was stuck at some point during the NCC deposition, resulting in less NCC bound and hence a lesser amount of GFP-CBM3a bound to that area as well. (Scale bar, 500  $\mu$ m.) (D) AFM image ( $3 \times 3 \mu$ m) of the NCC film deposited on a glass slide showing a densely covered surface. The red line represents the area used to obtain the average height profile trace shown below. Despite minor aggregation of NCC crystals during layer-by-layer deposition, height differences are less than 20 nm.

imaged by AFM; additional AFM images of bare and PLL-treated surfaces are found in *SI Appendix, Fig. S1*. Similar to spin-coated samples (50, 51), the surface was uniformly covered with NCC. AFM image analysis revealed the formation of NCC crystal aggregates at multilayered films. This is reflected by a surface roughness factor ( $R_a$ ) that is marginally greater than 3 nm compared to less than 2 nm estimated for a single NCC layer.

**Observation of Shortened DNA Tethers on NCC Surfaces.** The tether preparation method and analysis of traces, as outlined in *Materials and Methods*, were validated by tethering beads anchored to the AFS chip surface by anti-DIG antibodies (aDIG). The dimensionless contour length ( $l_{fc}$ ) of DNA tethers bound to aDIG during force calibration was  $1.1 \pm 0.12$  (mean  $\pm$  SD,  $n = 156$ ). This is in the expected range, given the particle size distribution of the beads. The average rupture force of the DIG–aDIG complex was determined to be  $18.8 \pm 7.0$  pN at a loading rate of  $0.14 \pm 0.05$  pN/s (*SI Appendix, Fig. S2*) and is close to the reported value of 16.6 pN at 0.11 pN/s (36). As shown in Fig. 3*A*, overstretching of the DNA tether was observed at  $\sim 65$  pN, thus confirming the formation of single tethers with the bead preparation method outlined in *Materials and Methods*. In contrast, the observed dimensionless tether length of DNA for NCC–CBM–tethered beads was only  $0.83 \pm 0.23$ , indicating a shortening of the tethers by  $\sim 25\%$ . However, the force–distance (FD) curves obtained during the linear force ramp follow the extensible worm-like chain (52) or WLC

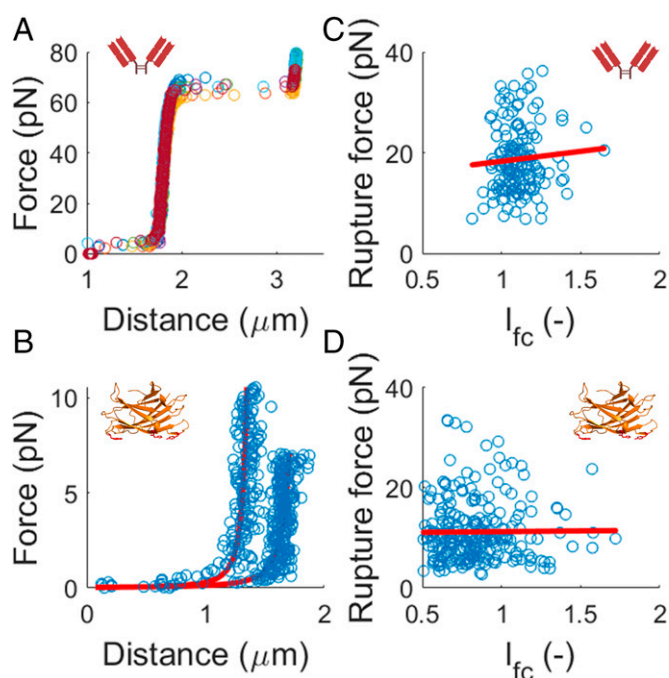


**Fig. 3.** No correlation was observed between tether length and rupture force for DIG–aDIG and CBM3a–cellulose interactions. (A) FD curves of DNA anchored to the chip surface by the DIG–aDIG bond ( $n = 7$ ). The extension at  $\sim 65$  pN is characteristic for a single DNA tether and indicates overstretching of DNA. (B) Example of FD curves for DNA anchored to the chip surface by the NCC–CBM bond. The red line shows the WLC fit with  $l_p = 42$  nm and  $S = 1,300$  pN. Despite following the WLC model, the tethers show a reduction in length of 25% on average. No overstretching was observed, since CBMs detach from the surface well below 65 pN. (C) Scatterplot and linear fit (red line) of rupture force and dimensionless length during force calibration ( $l_{fc}$ ) for DIG–aDIG ( $n = 156$ ). (D) Scatterplot and linear fit (red line) of rupture force and  $l_{fc}$  for CBM3a–wt at 1 pN/s ( $n = 259$ ). No significant correlation is found between the measured rupture force and  $l_{fc}$  (*SI Appendix, Tables S1 and S2*). The insets in A, C and B, D symbolize the aDIG antibody and CBM3a, respectively.

model (Fig. 3*B*), indicating that the tethers are only shortened but not otherwise altered. Fig. 3*C* and *D* shows the scatter plots of the rupture force with  $l_{fc}$  for DIG–aDIG and NCC–CBM3a–wt at 1 pN/s, respectively. The best linear fit (red line) is added as a guide. Additional scatter plots of root-mean-square fluctuation (RMS) and symmetrical motion (Sym) as well as the Pearson and Spearman correlation coefficients can be found in *SI Appendix, Fig. S3* and *Tables S1 and S2*. Except for the Pearson coefficient for Sym and rupture force of Y67A at 0.1 pN/s ( $P = 0.043$ ), no significant correlation ( $P < 0.05$ ) was identified between the measured rupture force and observed length as well as RMS and Sym. We hypothesize that the 1.8- $\mu\text{m}$ -long and flexible DNA tether wraps around and/or binds to exposed and weakly bound NCC crystals during the incubation step or that NCC somehow binds to the DNA, which shortens the apparent contour length. The attached NCC crystals are subsequently detached from the NCC surface when the bead is being pulled away from the surface during force calibration but stay bound to the DNA. Nonspecifically tethered beads were observed in control experiments with blank Ni-NTA and GFP tagged beads. However, the number of tethered beads was higher by at least 4 $\times$  for CBM-tethered beads. A schematic describing nonspecifically tethered beads can be found in *SI Appendix, Fig. S4*. The loss of tethered beads during the flushing step before bead tracking was noted in all cases but was significantly larger for non-CBM-tethered beads, further indicating weaker, nonspecific binding interactions of the DNA to NCC. The rupture force distribution of only tethers close to the expected length and the entire expected single-molecule tethers are identical, as can be seen in *SI Appendix, Fig. S5*, implying that a single CBM–NCC rupture event was measured even though a shortened tether was observed. Assuming that a single CBM was tethered when the FD curve follows the WLC model, the force calibration and rupture force determination were not affected by the shortening of DNA, and the data were included in all further analyses.

**Rupture Force Analysis and Application of the Dudko–Hummer–Szabo Model.** The rupture force distributions for CBM3a–wt and its Y67A mutant at a loading rate of 1 and 0.1 pN/s are shown in Fig. 4. The histogram bin width was chosen based on the Freedman–Diaconis rule (53), since the data deviate from a single normal distribution. To capture the apparent multimodal distribution, a double normal distribution was fit to the histogram. The means and SDs are summarized in *SI Appendix, Table S3*. Although the first mean is similar for WT (8.5 pN) and Y67A (7.9 pN) at 1 pN/s, there is a clear single rupture force peak observed for the Y67A mutant, but not for the WT. This difference is even more pronounced when comparing the rupture force distributions at 0.1 pN/s. Two distinct rupture force peaks were observed for the WT at 3.5 and 7.1 pN, respectively, whereas Y67A showed only one peak at 4.5 pN. All histograms show a “tail” toward larger rupture forces, which is defined by the second normal fit. At 1 pN/s, CBM3a–wt shows a distinct peak at 17.5 pN, followed by a long tail up to 35 pN, whereas no clear second peak but only a tail until 25 pN was observed for Y67A.

Fig. 5*A* and *B* shows the transformation of rupture force histograms to force-dependent bond lifetime data using Eq. 1 (circles) and the fit of Eq. 2 (solid lines) of the Dudko–Hummer–Szabo (DHS) model (54, 55) described in *Materials and Methods*, for WT and Y67A, respectively. Data from rupture force histograms obtained at different loading rates should fall on the same master curve for force-dependent bond lifetimes as predicted

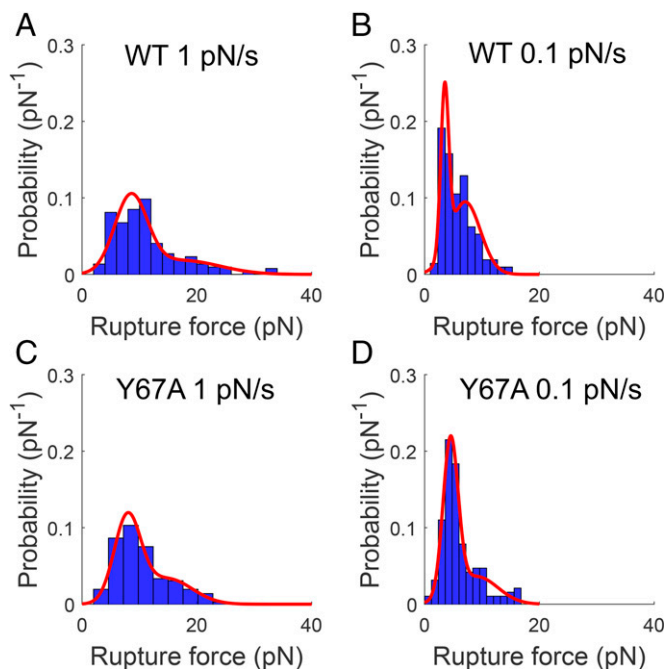


**Fig. 4.** AFS reveals distinct multimodal CBM–cellulose rupture force distribution at lower loading rates. (A and B) Obtained rupture force histograms and fit to a double normal distribution for CBM3a-wt at a loading rate of 1 pN/s ( $n = 259$ ) and 0.1 pN/s ( $n = 161$ ), respectively. (C and D) Rupture force histograms and fit to a double normal distribution for CBM3a Y67A at a loading rate of 1 pN/s ( $n = 138$ ) and 0.1 pN/s ( $n = 159$ ). The fit parameters are summarized in *SI Appendix, Table S3*. The tail toward higher rupture forces is observed in all cases; however, the Y67A mutant displays only a single peak at both loading rates, whereas CBM3a-wt shows no clear single peak, but rather two or more rupture force peaks.

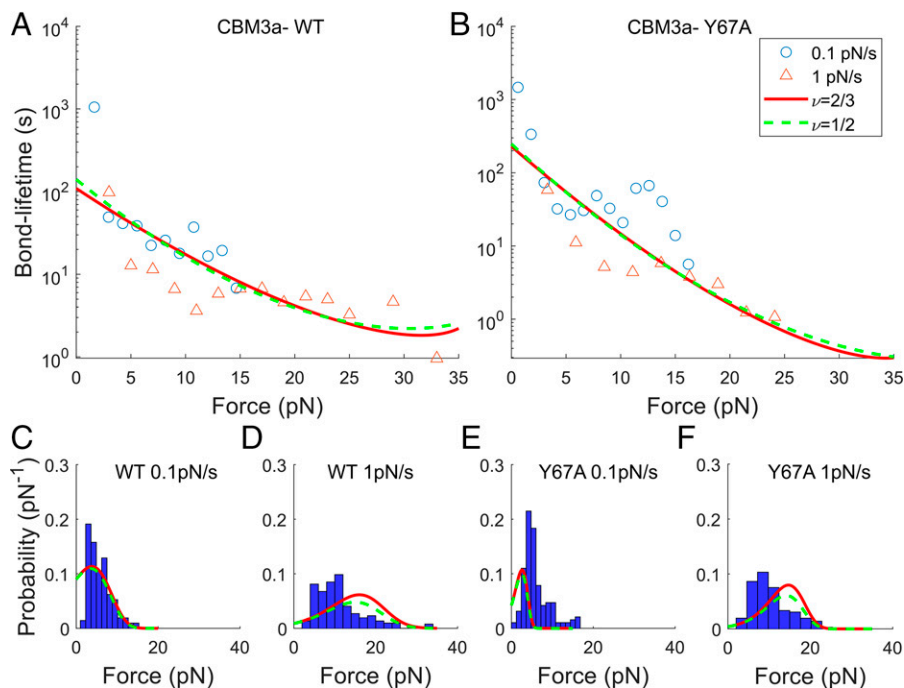
by Eq. 2 if the unbinding kinetics at constant force follow a single exponential function (55). Although there is some overlap of bond lifetimes obtained at 0.1 and 1 pN/s for both WT and Y67A, the fit of Eq. 2 inadequately describes the data for both shape factors  $\nu$ . A similar observation of bond lifetime data not following classical models was made recently for another type A CBM1 and its Y31A mutant using OTs (35), although the force-dependent bond lifetime was obtained in force-clamp mode. Surprisingly, no significant difference in the force-dependent bond lifetime was found between CBM1 and its Y31A mutant for most rupture forces. Fig. 5 C–F shows the rupture force histograms of WT and Y67A and the predicted probability density according to Eq. 3. Both shape factors produce a qualitatively similar probability distribution but insufficiently replicate the measured rupture forces. The main reason for discrepancies in bond lifetime and rupture probability distribution fit is the shape of the underlying rupture force histogram. Both the WT and Y67A rupture force histograms show tailing toward higher rupture forces with no clear peak, which results in almost force-independent bond lifetimes at higher rupture forces. The multimodal distribution observed for WT at both loading rates results in bond lifetime data not exactly following a single exponential decay function. As shown in Table 1, only  $\nu = 2/3$  yields unity for the numerical approximation of  $\int p(f)df$  over the modeled force range, despite qualitatively similar fits of the bond lifetime data and probability density for both shape factors. The extrapolated unbinding rates ( $k_{off}$ ) at zero force and  $\nu = 2/3$  for the WT is  $0.0091 \text{ s}^{-1}$  and approximately twice as high as the  $k_{off}$  for Y67A at  $0.0044 \text{ s}^{-1}$ . The unbinding rate of CBM3a-wt from sulfuric acid–derived microfibrils isolated from poplar and extracted from AFM–SMFS rupture force data using Bell’s model was estimated to be  $0.0089 \text{ s}^{-1}$  (34) and is close to the value obtained in our study.

Table 1 summarizes the fit parameters from Eq. 2 as well as the numerical approximation of  $\int p(f)df$  for both loading rates. The transition state distance,  $x^\ddagger$ , is 0.88 and 1.12 nm for WT and Y67A, respectively, and agrees with a transition state distance based on Bell’s model of 0.63 nm for CBM3a-wt (34). The apparent free energy of activation,  $\Delta G^\ddagger$ , is  $5.4 k_B T$  and  $8.1 k_B T$  for CBM3a-wt and Y67A, respectively, and contrasts with the  $45.3 k_B T$  previously reported (34). Both  $x^\ddagger$  and  $\Delta G^\ddagger$  are similar for the WT and mutant, indicating a similar unbinding pathway. The Bell and DHS models assume a one-dimensional unbinding pathway, which may not represent the underlying molecular interactions based on the multimodal rupture force distributions measured in this study, as well as evidence of different CBM binding orientations to crystalline cellulose that give rise to multiple nonequivalent binding sites (35, 56).

**Bulk Ensemble CBM3a Nanocellulose Off-Rate Qualitatively Agrees with AFS Results.** QCM-D experiments using hydrochloric acid–derived NCC as substrate reported a 1.4-fold increase in the off-rate for the Y67A mutant compared to the WT (20). However, using sulfuric acid–derived NCC, our QCM-D analysis using a classical one-site binding site adsorption model yielded a  $k_{off}$  of  $26.8 \pm 2.4 \times 10^{-5} \text{ s}^{-1}$  (mean  $\pm$  SD,  $n = 2$ ) and  $19.7 \pm 1.2 \times 10^{-5} \text{ s}^{-1}$  for WT and Y67A, respectively. This result supports the findings from AFS experiments that the WT unbinds more frequently, although the absolute values differ between AFS and QCM-D. In contrast, the number of available binding sites determined by QCM-D reduced from  $306 \pm 41 \times 10^{12}$  molecules to  $177 \pm 43 \times 10^{12}$  molecules between WT and Y67A, respectively.

**Molecular Simulations Reveal Stabilizing Role of Y67 on CBM3a Binding Mechanism.** All-atom MD simulations were performed with CBM3a-wt and Y67A mutant aligned on a cellulose I crystal such that the vector formed between W118 and Y67 points to the reducing end of the glucan chain (Fig. 6A). An equilibrated configuration is provided in Fig. 6B highlighting the amino acids of the CBM3a-wt planar binding motif with larger probability of interaction with cellulose (using a cut-off of 0.35 nm). In addition to the preserved  $CH - \pi$  forces arising from residues W118, H57, and Y67, several H bonds are formed between adjacent polar residues and the substrate, as identified previously (19). Fig. 6C summarizes the time-averaged H-bond formation between residues and the cellulose surface for WT and mutant. Changes in H-bond formation are observed with CBM residues S9, N10, N16, and D56, which is indicative of the alteration of the H-bond network due to the Y67A mutation.

Further analysis suggests that the observed alteration of the H-bond network between WT and mutant could be associated with a change in the orientation of the CBM with respect to cellulose. To examine the overall association of the CBM to cellulose, we computed the orientation of the CBM with respect to the cellulose surface. We defined an orientational angle ( $\theta$ ) as the vector formed between alpha carbons of residues W118 and Y67 and the normal vector of the cellulose plane (Fig. 6A). Notably, the average orientational angle for the WT is close to an orthogonal configuration ( $93.0 \pm 2.8^\circ$ , mean  $\pm$  SD) indicative that W118 and Y67 are perfectly aligned with respect to the water–cellulose interface. However, the Y67A mutation leads (on average) to an imperfect alignment ( $100.6 \pm 3.3^\circ$ ), with episodes of spontaneous partial detachment, indicated by angles as large as  $114^\circ$  (*SI Appendix, Fig. S7*).



**Fig. 5.** Application of the DHS model to obtained CBM3a-cellulose rupture forces highlights limitations of classical theory to study multivalent protein-polysaccharide unbinding interactions. (A and B) Force-dependent bond lifetime obtained from transforming rupture force distributions at 0.1 pN/s (o) and 1 pN/s ( $\Delta$ ) using Eq. 1 for WT and Y67A, respectively. The fit of Eq. 2 is shown for  $\nu = 2/3$  (red, solid line) and  $\nu = 1/2$  (green, dashed line). (C-F) Rupture force distributions at 0.1 and 1 pN/s with the fit of Eq. 3 for WT and Y67A, respectively, using the parameters obtained from fitting Eq. 2 to data in A and B for  $\nu = 2/3$  (red, solid line) and  $\nu = 1/2$  (green, dashed line). While both shape factors yield a qualitatively similar fit, only  $\nu = 2/3$  results in  $\int p(f)df = 1$ .

Interestingly, the Y67A mutation not only affects the association with cellulose but also leads to intramolecular rearrangement of residues within the CBM binding motif. Specific intramolecular H bonds in the aromatic binding motif of CBM3a are summarized in Fig. 6D. The Y67 mutation results in the total disruption of the H bond between residues 57 and 67, enabling the imidazole group of H57 to flip  $\sim 180^\circ$  with respect to the surface more frequently (SI Appendix, Fig. S6). This alternative configuration decreases the formation of H bonds between H57 and Q110, contrasting with the observed behavior seen in the WT. The H-bond formation of Q110 with the substrate remains similar for both proteins, indicating that the Y67 mutation does not have an impact on this residue. The overall loss in hydrogen bonding involving H57 for the mutant likely facilitates neighboring residue D56 to play a more prominent role, in terms of its H bonding to cellulose as well as its intramolecular H bonding with R112. Thus, MD simulations can capture the intricate rebalancing of intramolecular interactions within the CBM binding motif, due to the substitution at Y67 position, which also correlates with altered mutant CBM binding interactions with cellulose.

**Table 1. Fit parameters of force-dependent bond lifetimes for CBM3a-wt and Y67A mutant**

	$\nu$	$k_{off}$	$x^\ddagger$	$\Delta G^\ddagger$	$\int p(f)df$ at 0.1 pN/s [1 pN/s]
	(-)	( $s^{-1}$ )	(nm)	( $k_B T$ )	(-)
WT	2/3	0.0091	0.88	5.4	1.0 [1.0]
	1/2	0.0071	1.24	5.9	0.95 [0.80]
Y67A	2/3	0.0044	1.12	8.1	1.0 [1.0]
	1/2	0.0041	1.22	8.7	0.93 [0.79]

The integral column refers to the numerical integration of the rupture force probability as described by Eq. 3 in Materials and Methods for both loading rates.

## Discussion

We established a layer-by-layer deposition method for immobilizing NCC onto microfluidic chip surfaces and determined single-molecule CBM-cellulose unbinding forces at varying loading rates using AFS. Any soluble or insoluble polysaccharide substrate that can be spin-coated on glass surfaces, and is small enough not to clog the flow channel, can be readily immobilized within the AFS microfluidic chip using our proposed approach. Examples include the immobilization of regenerated cellulose, cellulose microfibrils, or chitin nanocrystals (30, 57, 58). Cellulose nanocrystals offer an especially promising platform for further chemical modifications (59, 60) either before or after immobilization to fine-tune protein adsorption (61), allowing the use of SMFS to a wider range of applications. Furthermore, a robust method for preparing tethered beads based on the well-known biotin-streptavidin and His-Ni-NTA interactions is presented here. Histidine tags are widely used to purify heterologously expressed proteins. Therefore, our proposed one-step tether synthesis via PCR with biotin- and NTA-modified primers is a convenient method to characterize most heterologous proteins for SMFS without further modifications.

Both the CBM3a-wt and Y67A mutant are fused to GFP on their N termini, which is located on the opposite side of the aromatic binding motif. The force-loading geometry (pulling from C vs. N terminus) can influence the measured rupture forces. For example, the biotin-streptavidin unbinding forces are reduced  $\sim 50\%$  when pulling from the N terminus compared to the C terminus, due to the partial unfolding of the N terminus (62). In the same study, it was shown that the attachment configuration influences the width of the rupture force distribution due to nonspecifically bound streptavidin. Although the unfolding force of CBM3a was not determined at the loading rates used in our experiments, it is unlikely that the CBM unfolds at forces of  $< 30$  pN, given its high mechanical

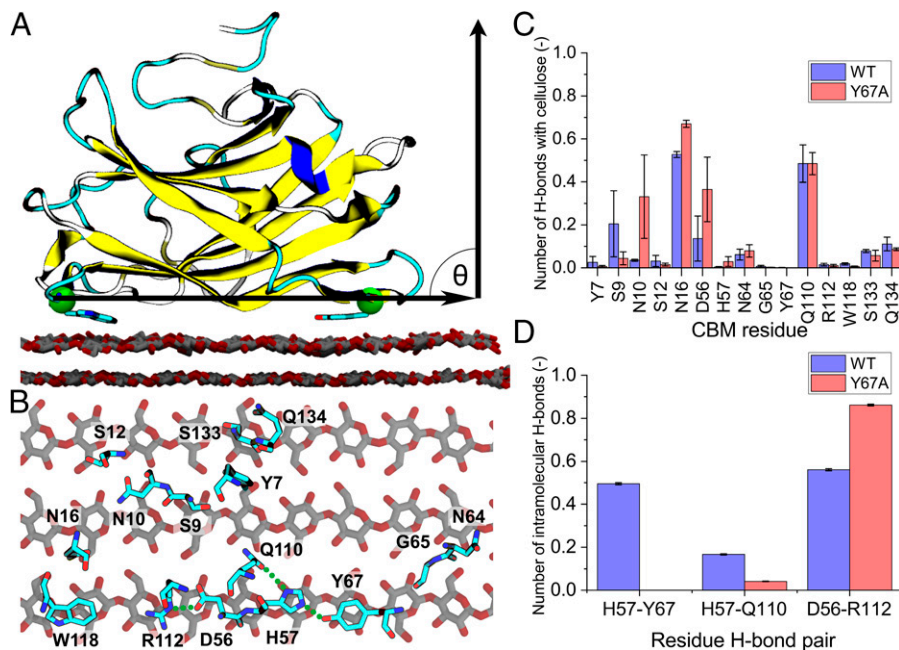


**Fig. 6.** MD simulations provide structural insights into the multiple interactions of CBM3a residues with the cellulose surface. (A) Representative configuration of CBM3a-wt interacting with the cellulose crystal as obtained from unbiased MD simulations. The vector formed between the C $\alpha$  of W118 (left green sphere) and C $\alpha$  of Y67 (right green sphere) indicates the horizontal alignment of the CBM toward the reducing end of the crystal. The angle between this vector and the normal vector of the surface is defined as  $\theta$ . (B) Close-up top view of the planar binding motif residues of CBM3a-wt identified to be in close contact with cellulose during MD simulations. Backbone and hydrogen atoms were omitted for clarity. Select interresidual H bonds are indicated by the dotted green line. (C) Comparison of average number of H bonds with cellulose for CBM3a-wt and Y67A mutant residues. Reduction in S9 seems to be compensated by increased stabilization for N10, N16, and D56 in the mutant. (D) Average intramolecular H-bond formation between pairs of amino acids in both the WT and Y67A mutant. The Y67A mutation leads to the total bond rupture between the H57 and A67 pair; however, significantly greater interactions are observed between D56 and R112. Error bars in C represent the average deviation of all trajectories of two independent simulations, and error bars in D are SEM.

stability (63). Even if partial unfolding would occur, it is expected that the protein should detach at lower forces, which was not observed in our study. In our tether attachment configuration, the (nonspecific) binding probability due to DNA or GFP binding to NCC is low compared to CBM tethers. The dsDNA only weakly binds to cellulose (64) in solution; however, certain single-stranded DNA fragments engineered as binding aptamers have been shown to specifically bind to cellulose (65). Since we use dsDNA in our assay, we can rule out any significant interference of DNA–cellulose interaction on the observed rupture forces. Furthermore, CBM tethers binding to weakly bound NCC crystals are most likely removed during the flushing step or the AFS force calibration step. Thus, weakly bound NCC crystals can be eliminated as a potential source for the observation of larger rupture forces seen during our study.

Analysis of the rupture force distribution reveals distinct differences between CBM3a-wt and its Y67A mutant. The fact that no rupture forces greater than 25 pN were measured for Y67A at 1 pN/s could be related to the difference in sample size ( $n = 259$  vs.  $n = 138$  for WT and Y67A, respectively), as the tail of larger rupture forces at 0.1 pN/s is similar for WT and Y67A ( $n = 161$  vs.  $n = 159$  for WT and Y67A, respectively). A similar shape of rupture force distributions was observed in previous AFM-based studies for CBM3a (33) and CBM1 (30, 66), but previous AFM analysis also found a more Gaussian-like distribution for CBM3a (31, 34). King et al. (33) showed that specific binding of CBM3a can be blocked with the addition of NCC and restored by washing the CBM-functionalized AFM tip with an excess of water. In that previous study, both the initial and restored rupture force distributions displayed tailing, suggesting that nonspecific binding was likely

not the reason for the observation of higher rupture forces as seen in our case.

The tailing of the rupture force distributions toward larger rupture forces may also be correlated with the naturally evolved role of the CBM for proper functioning of the cellulosome. As cellulosomal microbes colonize cellulosic substrates, they are subjected to high interfacial shear forces, for example, in the gut–intestine of higher organisms (67). The main cellulosomal scaffold protein, cohesin, is relatively stable and unfolds only under forces greater than 140 pN (68, 69), leaving the interdomain CBM mostly intact (63). Depending on the pulling speed and complex-stabilizing neighboring modules, the cohesin–dockerin interaction, which tethers cellulases to the scaffold, shows multiple unbinding modes with catch bond behavior (63, 70, 71). A similar response to external forces is hypothesized to be found in other scaffold units such as the CBM. Thus, CBMs may have also evolved to remain bound to cellulose during elevated levels of mechanical stress, but remain flexible enough for the cellulosome to adopt to different bound conformations on the cellulose surface to facilitate substrate hydrolysis (11, 72). This flexibility could be reflected in our observed broad and bimodal rupture force distribution and the failure of the DHS model to predict the unbinding rate at zero force. Nevertheless, multivalency, which can also take the form of multiple CDs interacting with the substrate, may be as important in withstanding mechanical stress, but this has not yet been adequately characterized in the literature.

Surface diffusion of cellulases on crystalline cellulose was experimentally verified, although the extent of surface diffusion was minor compared to dynamic CBM-driven binding and unbinding of cellulases to the substrate (73, 74). To date, no motility or processive motion has been observed experimentally

for CBMs without being tethered to a CD. However, a computational study of CBM1 from *T. reesei* revealed that CBM1 can diffuse from the hydrophilic to the hydrophobic surface of a cellulose I crystal, during which multiple local energy minima with distinct orientations were sampled (56). Similarly, it has been shown that CBM1 can bind in a noncanonical orientation to cellulose III (35), which indicates that type A CBMs potentially display a much larger range of binding orientations on crystalline cellulose surfaces. Single-molecule imaging found that CBM1 exhibits distinct surface binding events (28), which could be correlated to distinct regions of crystalline cellulose, and such binding modes may potentially also be found in other type A CBMs such as CBM3a. When fused to an endoglucanase, CBM3a occupies more binding sites on crystalline cellulose compared to CBM1 fused to the same CD, further suggesting the presence of specific binding sites accessible to different type A CBMs (75).

The Y67A mutation is located at the edge of the binding site of CBM3a, thus reducing and disrupting the effective total planar binding motif available for multimodal binding interactions with cellulose. Our MD simulations showed that the absence of Y67 “tilts” the whole CBM toward W118, resulting in more frequent H-bond formation between polar residues and the substrate. While MD simulations were carried out using an ideal native cellulose crystal, these results indicate a somehow compensatory effect due to enhanced H-bond formation. In our experiments, in addition to the nonideal crystallinity, the sulfuric acid-derived NCC also displays sulfate groups on the surface (0.3  $\mu\text{mol}$  sulfur per mg dry NCC). Thus, the mutant could additionally engage with these charged sulfate groups, compensating for the loss of  $\pi$ -stacking forces. These interactions may recover the affinity, resulting in similar off-rates and unbinding forces of WT and mutant, contrasting a previously reported reduction in off-rate for the same mutant using hydrochloric acid-derived NCC (20). However, binding orientations which were determined or stabilized by the Y67–substrate interaction may no longer be favorable in the absence of this residue, as we observed a reduction in total available binding sites by 1.8-fold, despite similar unbinding rates determined by QCM-D.

In summary, based on insights from AFS assays and MD simulations, we hypothesize that the planar aromatic binding motif of CBM3a can be grouped into two regions, as highlighted in Fig. 7 as blue and red regions. The first region is dominated by the interactions of W118 and R112/D56 with the substrate, whereas the second region is established by H57 and Y67 interactions with the substrate. For the WT, both regions are intact. Thus, pulling on the protein results in a bimodal distribution, depending on which region is first dissociated from the cellulose surface. In contrast, the interaction with the substrate of the second region for the mutant (highlighted in red in Fig. 7) is greatly reduced due to the significantly higher tilt angle, thus resulting in a unimodal rupture force distribution. Alternatively, the CBM may also take on additional binding orientations on the crystalline surface, where binding residues may span across multiple glucan chains, in addition to binding along a single glucan chain. Even in such a case with more complex binding modes considered (i.e., analogous to Buffon’s needle model for multiple CBM–cellulose binding modes), the unbinding force may differ between on-chain and across-chain binding events, which still may be differentiated using SMFS (35). To further understand the role of each binding residue in recognizing and dissociating from the substrate, rupture force measurements and MD simulations of other mutants (such as H57 or W118 mutated to alanine) are suggested in future studies. While the application of the DHS model for CBM3a-wt yielded an

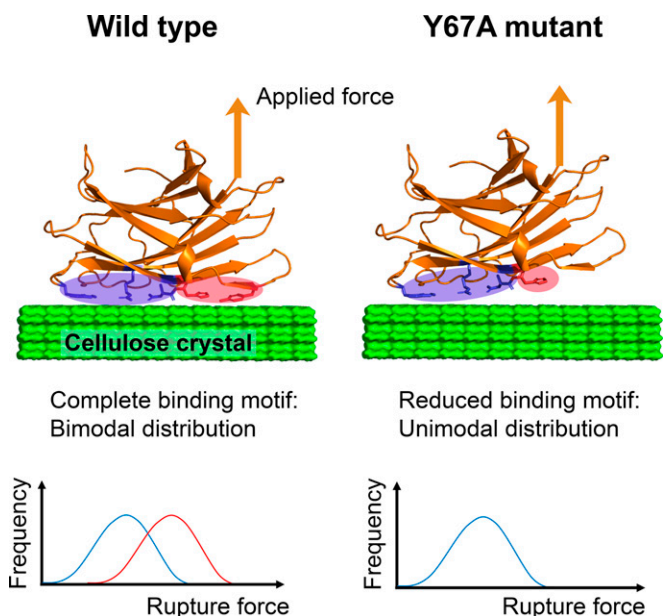


**Fig. 7.** Summary of hypothesized origin of multimodal rupture force distribution observed for CBM3a-wt bound to cellulose. The planar binding motif may be grouped into two regions, as highlighted in blue and red oval regions shown here. For CBM3a-wt, both regions are intact and interacting with the surface in a multimodal manner. Hence, pulling on the protein yields a bimodal rupture force distribution, depending on which region ruptures from the surface first. The Y67A mutant binds to the cellulose crystal slightly tilted, reducing the interactions between the red region and the substrate. Applying a force on the mutant may therefore result in a unimodal rupture force distribution, since only the blue binding region highlighted is fully engaged with the substrate at any given point in time.

unbinding rate comparable to previous SMFS results, such classical models still failed to accurately predict the unbinding rate of the Y67A mutant as well as describe the broad rupture force distribution with the obtained fit parameters for both proteins. This issue might be resolved if bond lifetime measurements are carried out in force-clamp mode rather than transforming rupture force histograms to bond lifetime data. Nevertheless, rupture force histograms could be used further to evaluate the existence of a catch bond behavior for CBMs. Understanding the influence of each binding residue on the binding and unbinding rate will pave the way for rational engineering approaches to fine-tune CBM–substrate interactions for optimized catalytic activity of cellulases and cellulosomes. This will also open up new avenues for CBM utilization, such as nanomaterials (76) or as interfacial anchors for cell immobilization (77). Similar studies using multiplexed SMFS will deepen our fundamental understanding of the complex multimodal interactions between a wide range of proteins with carbohydrates at interfaces, and the functional role of such biophysical interactions in biology.

## Materials and Methods

**Chemicals and Substrates.** Unless otherwise mentioned, all reagents were either purchased from VWR International, Fisher Scientific, or Sigma-Aldrich. Streptavidin-coated polystyrene particles (SVP30) with a nominal diameter of 3.11  $\mu\text{m}$  were purchased from SpheroTech Inc. Amino-functionalized beads (01-01-503) with a nominal diameter of 5  $\mu\text{m}$  were purchased from Micromod Partikeltechnologie GmbH and used as fiducial beads to account for drift during AFS assays. Sulfuric acid-hydrolyzed NCC was kindly donated by Richard Reiner, USDA Forest Product Laboratory, Madison, Wisconsin. (78).

**DNA Tethers.** Linear dsDNA tethers were synthesized in one step by PCR using the pEC-GFP-CBM3a plasmid as a template and 5' modified primers. The biotin-modified primer (forward primer, 5'-biotin-C6-GGCGATCGCCTGGAAGTA) was

purchased from Integrated DNA Technologies, Inc. The NTA-modified primer (backward primer, 5'-NTA-SS-C6-TCCAAAGGTGAAGAACTGTTCCACC) was purchased from Gene Link, Inc. The whole plasmid (5.4 kb) was amplified, then purified using the PCR Clean-up kit (IBI Scientific), resulting in a linear DNA tether of  $\sim 1.8\text{-}\mu\text{m}$  length with one modification on each end of the DNA. Amplification and product purity was verified by gel electrophoresis. In addition, a linear DNA tether of the same length was amplified using a digoxigenin-modified primer instead of NTA (5'-DIG-NHS-TCCAAAGGTGAAGAACTGTTCCACC, Integrated DNA Technologies, Inc.) to bind to aDIG Fab fragment antibodies (11214667001, Roche).

**Proteins.** His<sub>8</sub>-GFP-CBM3a WT and its Y67A mutant were expressed and purified as described previously (20).

**Buffers.** All AFS experiments were carried out in working buffer (WB) containing 10 mM phosphate buffer at pH 7.4 supplemented with 0.31 mg/mL bovine serum albumin (BSA) and casein and 0.19 mg/mL Pluronic F-127, respectively. In addition, two blocking buffers were used to passivate the surface before the experiment. Buffer B1 consists of 10 mM phosphate buffer supplemented with 2.5 mg/mL BSA and casein. Buffer B2 consists of 10 mM phosphate buffer supplemented with 2.2 mg/mL BSA and casein and 5.6 mg/mL Pluronic F-127, respectively. All buffers were degassed in a vacuum ( $-90\text{ kPa}$ ) for 30 min.

**QCM-D Experiments.** QCM-D experiments were carried out and analyzed as described previously (20) except for using 10 mM phosphate buffer at pH 7.4 and sulfuric acid-derived NCC.

**Atomistic MD Simulations of CBM3a Interacting with Cellulose.** Initial coordinates of cellulose I were built using a cellulose builder script (79). The fiber was constructed to generate a parallelepiped geometry with crystalline parameters 4 4 5. Initial coordinates of CBM3a were downloaded from the Protein Data Bank (PDB) (ID: 4JO5), and missing sidechains were reconstructed using the Chimera molecular viewer with the most populated rotameric configurations based on the Dunbrack database (80). All simulations were carried with the Amber16 molecular dynamics package (81), and spatial coordinates were collected every 100 ps for analysis. A detailed description of the system setup as well as MD protocol is provided in *SI Appendix*. Initial and final MD simulation configurations of WT and Y67A mutant interactions with the cellulose surface are provided in rtf format as *SI Appendix*.

**Cellulose Film Preparation and AFS Chip Cleaning.** The microfluidic chips used in the AFS are custom designed by LUMICKS B.V. for reuse. Therefore, a reliable protocol for the immobilization and removal of NCC needed to be established. A multilayer deposition process (50) using an automated microfluidic control system was employed from Elveesy S.A.S. to obtain a stable cellulose film. The system consists of a microfluidic controller (OB1, driven by compressed nitrogen), a 10-port distribution valve (MUX-D), pressurized fluid reservoirs (2 mL to 50 mL), and a manifold. To avoid potential damage to the 10-port valve when in contact with NCC, the valve was used to direct the pressurized nitrogen to the correct reservoir instead of directly controlling the liquid streams. Due to this configuration, installing check valves on each line was necessary prior to entering the manifold to avoid backflow and cross-contamination between reservoirs. The flowsheet of the setup is shown in Fig. 2 A and B, and the detailed part list can be found in *SI Appendix, Table S4*. The microfluidic resistance of the setup including the AFS chip was determined to be  $3\text{ }\mu\text{L}/(\text{min}\cdot\text{mbar})$ , and the volume flown through the chip was calculated based on the set pressure and duration. First, the cleaned chip was rinsed with 2 mL of deionized (DI) water, followed by flushing through 200  $\mu\text{L}$  of 0.05% (wt/vol) PLL and incubation for 1 min. Next, the chip was rinsed with 1 mL of DI water and blow-dried for 1 min. Then 200  $\mu\text{L}$  of NCC at a concentration of 0.5% (wt/vol) was incubated for 1 min, followed by 1-mL water rinse and drying for 1 min. The deposition of PLL and NCC was repeated four more times. Following the final NCC layer deposition, the chip was blow-dried for 20 min. Finally, the chip was disassembled, and the bottom part, including the flow cell, was placed in an oven at  $50\text{ }^\circ\text{C}$  to dry up overnight.

To confirm cellulose deposition using AFM, flow cells of the same channel geometry as the AFS chips were prepared by cutting the channel from Parafilm and fixing it between two microscope slides. Holes were drilled in one slide to connect 1/16" outer diameter (1/32" inner diameter) polytetrafluoroethylene tubing. After assembly, the multilayer deposition process described above was

employed manually. The slides were taken apart and dried up overnight at  $50\text{ }^\circ\text{C}$  and stored in a desiccator until AFM imaging. The deposited NCC samples were visualized from the randomly selected area by an AFM (NX-10, Park systems). The AFM was used in noncontact mode operation with a scan size between  $2 \times 2\text{ }\mu\text{m}$  and  $5 \times 5\text{ }\mu\text{m}$ , 0.3-Hz scan rate, and 11.1-nm set point with the noncontact mode AFM tip (SSS-NCHR, Park Systems). The AFM images were analyzed using XEI software (Park Systems).

To directly verify the deposition of NCC inside the AFS chip, the fluorescence intensity of GFP-CBM3a-wt bound to NCC was measured. All experiments were carried in at least triplicate. The chip was first rinsed with 500  $\mu\text{L}$  of DI water and 500  $\mu\text{L}$  of phosphate buffer followed by 15 min of passivation of the surface in B1 and B2 buffer, respectively. GFP-CBM3a-wt was diluted in WB to a concentration of  $1\text{ }\mu\text{M}$  and incubated for 5 min, followed by rinsing in 1 mL of WB. The fluorescence images were taken with a complementary metal-oxide-semiconductor (CMOS) camera (Kiralux, Thorlabs Inc.) using  $\mu\text{Manager}$  (82) on an inverted fluorescence microscope (Olympus IX 71) equipped with the necessary filters to enable GFP fluorescence. Control experiments on bare glass and PLL-treated chip surfaces were performed to estimate the degree of nonspecific binding of GFP-CBM3a. All images were corrected for background and shading (83).

The NCC was removed by incubating piranha solution (7:3 concentrated  $\text{H}_2\text{SO}_4$ :30%  $\text{H}_2\text{O}_2$ , vol/vol) two times for 15 min to 30 min at  $50\text{ }^\circ\text{C}$  with 500- $\mu\text{L}$  DI water rinses in between. The next step in the cleaning procedure involved incubation of 1 M NaOH for 1 h to 12 h at room temperature followed by incubation of piranha solution for 15 min to 30 min at  $50\text{ }^\circ\text{C}$ , rinsing with 5 mL of DI water, and drying. If the AFS chips were used for single-molecule experiments, 5- $\mu\text{m}$   $\text{NH}_2$ -functionalized beads (to serve as fiducial beads) were diluted  $\sim 1$ :1,000 in 0.01 M HCl and dried up inside the chip overnight at  $50\text{ }^\circ\text{C}$  before the chip was functionalized with NCC.

**Tethered Bead Preparation for SMFS.** Single-molecule experiments were carried out on a G1 AFS instrument with G2 AFS chips provided by LUMICKS B.V. After immobilizing NCC, the AFS chip was rinsed with 500  $\mu\text{L}$  of DI water and 500  $\mu\text{L}$  of phosphate buffer. Next, the surface was passivated with B1 and B2 buffer for 15 min each and rinsed with WB. The NTA-DNA tethers were diluted to 6 pM in WB containing 6 nM  $\text{NiCl}_2$ . The bead-DNA-CBM construct was prepared in a two-step procedure. First, 15  $\mu\text{L}$  of streptavidin-coated beads and Ni-NTA-DNA tethers were mixed to yield less than one DNA tether per bead and incubated on a rotisserie for 30 min. Details about the specificity of the Ni-NTA moiety for His-tagged CBMs can be found in *SI Appendix, Fig. S8*, and the determination of the overall binding efficiency of DNA tethers to the beads is described in *SI Appendix*. The functionalized beads were washed twice by spinning down, removing the supernatant, and resuspending in 100  $\mu\text{L}$  of WB. GFP-CBM3a-wt or Y67A mutant were diluted to 2 nM in WB. The washed and DNA-functionalized bead pellet was resuspended in 20  $\mu\text{L}$  of either WT or Y67A solution (resulting in a  $>1,000\times$  molar excess of CBM with respect to DNA) and placed on the rotisserie for 30 min. Next, the beads were washed twice in WB to remove any unbound CBM and resuspended in 20  $\mu\text{L}$  of WB or B2 if a high nonspecific bead binding was observed during SMFS experiments. There was no significant difference in the partition coefficient between WB and B2 for WT ( $P = 0.68$ , degree of freedom [df] = 7) and Y67A ( $P = 0.49$ , df = 7) mutant. Refer to *SI Appendix* for information about the experimental setup, and refer to *SI Appendix, Fig. S9* for binding data. The CBM-DNA-bead construct was flushed through the AFS chip and incubated for 30 min. Nonbound beads were subsequently washed out with WB at a flow rate of 2  $\mu\text{L}/\text{min}$  using a syringe pump (New Era Pump Systems Inc.). A small force of  $\sim 0.2\text{ pN}$  to 0.5 pN was applied to speed up the flushing step. For illustration, a schematic of the single-molecule setup is shown in Fig. 1D. After measuring the rupture forces, the chip was rinsed with 100  $\mu\text{L}$  of WB, and the next CBM-DNA-bead sample was inserted.

To verify that the amplified DNA tethers are 1.8  $\mu\text{m}$  in length, aDIG fab fragments dissolved in PBS (20  $\mu\text{g}/\text{mL}$ ) were nonspecifically bound to the AFS glass surface for 20 min, followed by the same passivation procedure as outlined above. The DNA tethers in this experiment were functionalized with DIG instead of NTA (Fig. 1C). The DNA-to-bead ratio was between 5 and 10 to ensure a sufficient yield of single-molecule tethers. DNA-functionalized beads were incubated on the surface for 10 min to 30 min, and the flushing process, bead tracking, and analysis procedure were identical to CBM-tethered bead experiments.

**Bead Tracking, Force Ramp Application, and Determination of Rupture Forces.** Tracking and analysis of the beads were accomplished using the software package provided by LUMICKS, with slight modifications to allow efficient export of rupture forces and associated tether statistics, as well as FD curves, to a spreadsheet. The procedure for identifying a single-molecule tether, force calibration, and rupture force determination is described in detail elsewhere (36). The beads were tracked at 20 Hz using a 10× magnification objective. The trajectory of the beads without applied force was monitored for 8 min to 10 min to determine the point of surface attachment (anchor point). Next, the force on each bead was calibrated by applying a constant amplitude for 2 min to 4 min. Typically, two or three different amplitude values were used to build the calibration curve between the applied amplitude and effective force on each bead. Single-molecule tethers were identified by the RMS and Sym of the bead around the anchor point during the time frame for anchor point determination. For the CBM–cellulose experiment, values of single-molecule tethers for RMS and Sym are in the range between 850 and 1,200 nm and 1.0 and 1.3, respectively. During force calibration, the diffusion coefficient of the bead and the force were used as fit parameters. This diffusion coefficient was compared to the diffusion coefficient determined by the Stokes–Einstein relation and was in the range between 0.8 and 1.2 for single tethers. The force obtained during force calibration was used to estimate the theoretical extension of DNA using the extensible WLC model (52). This extension was compared to the measured length during that force calibration point to yield the dimensionless length  $l_{fc}$  and was expected to be close to one for single tethers. Next, a linear force ramp of either 0.1 pN/s or 1 pN/s was applied. Rupture forces were determined through the software by finding the time frame at which the z position of the bead was outside the interval covered by the lookup table value (36). An example time trace of a typical rupture force measurement is shown in *SI Appendix, Fig. S10*. Each trace and FD curve during force ramp application was inspected manually to determine the rupture force accurately.

**Analysis of Rupture Forces.** Further evaluation of traces as well as data analysis was carried out by a custom-written MATLAB script, as briefly described below. For each known single-molecule trace, several indicators such as RMS, Sym,  $l_{fc}$ , rupture force, and loading rate, along with the obtained FD curve during force ramp application, were imported into MATLAB. To each FD curve, the dimensionless contour length  $l_c$  of the WLC model based on the expected contour length of 1,800 nm was fitted using a persistence length of  $l_p = 42$  nm and stretch modulus  $S = 1,300$  pN (84). This fitted length (determined during the force ramp) was compared to the dimensionless length during force calibration  $l_{fc}$  and only traces close to one were further analyzed. The script also identified traces in which the rupture force or loading rate was 3 SDs away from the sample mean. Those traces were examined manually and discarded if the FD curve or any other mentioned statistics indicated that the trace did not originate from a single-tethered bead. To ensure that no bias was introduced by removing traces, the remaining data were subjected to a Pearson and Spearman correlation coefficient test between the obtained rupture force and RMS, Sym, and  $l_{fc}$ , respectively. Finally, the obtained rupture force histograms were converted to force-dependent bond lifetime data and analyzed using the procedure outlined by Dudko et al. (55) to obtain the bond lifetime in the absence of force. The

rupture force histograms were converted to force-dependent bond lifetime data using Eq. 1,

$$\tau(F_k) = \frac{\Delta F(h_k/2 + \sum_{i=k+1}^N h_i)}{h_k \dot{F}(F_k)}, \quad [1]$$

where  $\tau(F_k)$  and  $\dot{F}(F_k)$  are the average bond lifetime and loading rate at the  $k^{\text{th}}$  bin and  $F_k = F_0 + (k - 1/2)\Delta F$ . The rupture force histogram is composed of  $N$  bins of width  $\Delta F$  starting from  $F_0$  and ending at  $F_0 + N\Delta F$ . The number of counts in the  $i^{\text{th}}$  bin is  $C_i$ , and the height of each bin can be calculated as  $h_i = C_i / N_{\text{tot}} \Delta F$ , where  $N_{\text{tot}}$  is the total number of counts.

The force-dependent bond lifetime  $\tau(F)$  is described using Eq. 2,

$$\tau(F) = \tau_0 \left( 1 - \frac{\nu F x^\ddagger}{\Delta G^\ddagger} \right)^{1-1/\nu} e^{-\beta \Delta G^\ddagger \left[ 1 - \left( 1 - \frac{\nu F x^\ddagger}{\Delta G^\ddagger} \right)^{1/\nu} \right]}, \quad [2]$$

where  $\beta = 1/k_B T$ ,  $\tau_0 = 1/k_{\text{off}}$  is the bond lifetime (or inverse of the unbinding rate  $k_{\text{off}}$ ),  $x^\ddagger$  is the transition state distance, and  $\Delta G^\ddagger$  is the apparent free energy of activation in the absence of the external force. The shape factor  $\nu = 1/2$  or  $2/3$  describes the underlying free-energy profile as cusp or linear cubic, respectively.

The distribution of rupture forces is described by Eq. 3,

$$\rho(F) = \frac{1}{\dot{F}(F)\tau(F)} e^{-\int_0^F 1/\dot{F}(F)\tau(F) dF}. \quad [3]$$

**Data, Materials, and Software Availability.** All study data are included in the article and/or supporting information.

**ACKNOWLEDGMENTS.** S.P.S.C. acknowledges support from the National Science Foundation (NSF) (Chemical, Bioengineering, Environmental and Transport Systems [CBET] CAREER Award 1846797), Rutgers Aresty Research Center, and Rutgers Startup Funds. J.M.Y. was supported by the Department of Energy, Office of Energy Efficiency and Renewable Energy under Agreement 28598. K.-B.L. acknowledges partial support from the NSF (CBET-1803517), the New Jersey Commission on Spinal Cord (CSCR17IRG010 and CSCR16ERG019), and National Institutes of Health (NIH) R01 (1R01DC016612, 3R01DC016612-01S1, and 5R01DC016612-02S1). C.A.L. and S.G. acknowledge support from Los Alamos National Laboratory (LANL) Laboratory Directed Research and Development (LDRD) Exploratory Fund (ER) (XWX2) and LANL institutional program for computational resources. M.H. thanks Dr. Bhargava Nemmaru for his help with the QCM-D data analysis. Fig. 1 A, C, and D and *SI Appendix, Figs. S4, S8A, and S10A* were created using BioRender.com.

Author affiliations: <sup>a</sup>Department of Chemical and Biochemical Engineering, Rutgers, The State University of New Jersey, Piscataway, NJ 08854; <sup>b</sup>Department of Chemistry and Chemical Biology, Rutgers, The State University of New Jersey, Piscataway, NJ 08854; <sup>c</sup>Biosciences Center, National Renewable Energy Laboratory, Golden, CO 80401; and <sup>d</sup>Theoretical Division, Los Alamos National Laboratory, Los Alamos, NM 87545

1. N. Georgelis, N. H. Yennawar, D. J. Cosgrove, Structural basis for entropy-driven cellulose binding by a type-A cellulose-binding module (CBM) and bacterial expansin. *Proc. Natl. Acad. Sci. U.S.A.* **109**, 14830–14835 (2012).
2. D. J. Cosgrove, Loosening of plant cell walls by expansins. *Nature* **407**, 321–326 (2000).
3. L. Qin et al., Plant degradation: A nematode expansin acting on plants. *Nature* **427**, 30 (2004).
4. M. D. L. Suits et al., Conformational analysis of the *Streptococcus pneumoniae* hyaluronate lyase and characterization of its hyaluronan-specific carbohydrate-binding module. *J. Biol. Chem.* **289**, 27264–27277 (2014).
5. M. J. Jedrejzjas, Pneumococcal virulence factors: Structure and function. *Microbiol. Mol. Biol. Rev.* **65**, 187–207 (2001).
6. S. P. S. Chundawat, G. T. Beckham, M. E. Himmel, B. E. Dale, Deconstruction of lignocellulosic biomass to fuels and chemicals. *Annu. Rev. Chem. Biomol. Eng.* **2**, 121–145 (2011).
7. M. E. Himmel et al., Biomass recalcitrance: Engineering plants and enzymes for biofuels production. *Science* **315**, 804–807 (2007).
8. A. B. Boraston, D. N. Bolam, H. J. Gilbert, G. J. Davies, Carbohydrate-binding modules: Fine-tuning polysaccharide recognition. *Biochem. J.* **382**, 769–781 (2004).
9. C. M. Payne et al., Fungal cellulases. *Chem. Rev.* **115**, 1308–1448 (2015).
10. C. M. G. A. Fontes, H. J. Gilbert, Cellulosomes: Highly efficient nanomachines designed to deconstruct plant cell wall complex carbohydrates. *Annu. Rev. Biochem.* **79**, 655–681 (2010).
11. M. Eibinger, T. Ganner, H. Plank, B. Nidetzky, A biological nanomachine at work: Watching the cellulosome degrade crystalline cellulose. *ACS Cent. Sci.* **6**, 739–746 (2020).
12. E. A. Bayer, H. Chanzy, R. Lamed, Y. Shoham, Cellulose, cellulases and cellulosomes. *Curr. Opin. Struct. Biol.* **8**, 548–557 (1998).
13. R. H. Doi, A. Kosugi, Cellulosomes: Plant-cell-wall-degrading enzyme complexes. *Nat. Rev. Microbiol.* **2**, 541–551 (2004).
14. K. Igarashi et al., Traffic jams reduce hydrolytic efficiency of cellulase on cellulose surface. *Science* **333**, 1279–1282 (2011).
15. Y. Zhang, M. Zhang, R. Alexander Reese, H. Zhang, B. Xu, Real-time single molecular study of a pretreated cellulose hydrolysis mode and individual enzyme movement. *Biotechnol. Biofuels* **9**, 85 (2016).
16. Y. Shibafuji et al., Single-molecule imaging analysis of elementary reaction steps of *Trichoderma reesei* cellobiohydrolase I (Cel7A) hydrolyzing crystalline cellulose I $\alpha$  and III. *J. Biol. Chem.* **289**, 14056–14065 (2014).
17. B. W. McLean et al., Analysis of binding of the family 2a carbohydrate-binding module from *Cellulomonas fimi* xylanase 10A to cellulose: Specificity and identification of functionally important amino acid residues. *Protein Eng.* **13**, 801–809 (2000).
18. J. Kraulis et al., Determination of the three-dimensional solution structure of the C-terminal domain of cellobiohydrolase I from *Trichoderma reesei*. A study using nuclear magnetic resonance and hybrid distance geometry-dynamical simulated annealing. *Biochemistry* **28**, 7241–7257 (1989).

19. J. Tormo *et al.*, Crystal structure of a bacterial family-III cellulose-binding domain: A general mechanism for attachment to cellulose. *EMBO J.* **15**, 5739–5751 (1996).
20. B. Nemmaru *et al.*, Reduced type-A carbohydrate-binding module interactions to cellulose I leads to improved endocellulase activity. *Biotechnol. Bioeng.* **118**, 1141–1151 (2021).
21. D. Gao *et al.*, Increased enzyme binding to substrate is not necessary for more efficient cellulose hydrolysis. *Proc. Natl. Acad. Sci. U.S.A.* **110**, 10922–10927 (2013).
22. J. Kari *et al.*, Physical constraints and functional plasticity of cellulases. *Nat. Commun.* **12**, 3847 (2021).
23. D. W. Abbott, A. B. Boraston, Quantitative approaches to the analysis of carbohydrate-binding module function. *Methods Enzymol.* **510**, 211–231 (2012).
24. A. L. Creagh, E. Ong, E. Jervis, D. G. Kilburn, C. A. Haynes, Binding of the cellulose-binding domain of exoglucanase Cex from *Cellulomonas fimi* to insoluble microcrystalline cellulose is entropically driven. *Proc. Natl. Acad. Sci. U.S.A.* **93**, 12229–12234 (1996).
25. Y. Zhang *et al.*, Interactions between type A carbohydrate binding modules and cellulose studied with a quartz crystal microbalance with dissipation monitoring. *Cellulose* **4**, 3661–3675 (2020).
26. J. Guo, J. M. Catchmark, Binding specificity and thermodynamics of cellulose-binding modules from *Trichoderma reesei* Cel7A and Cel6A. *Biomacromolecules* **14**, 1268–1277 (2013).
27. S. J. Charnock *et al.*, Promiscuity in ligand-binding: The three-dimensional structure of a *Piromyces* carbohydrate-binding module, CBM29-2, in complex with cello- and mannohexaose. *Proc. Natl. Acad. Sci. U.S.A.* **99**, 14077–14082 (2002).
28. A. Nakamura *et al.*, Single-molecule imaging analysis of binding, processive movement, and dissociation of cellobiohydrolase trichoderma reesei Cel6A and its domains on crystalline cellulose. *J. Biol. Chem.* **291**, 22404–22413 (2016).
29. S. K. Brady, S. Sreelatha, Y. Feng, S. P. S. Chundawat, M. J. Lang, Cellobiohydrolase 1 from *Trichoderma reesei* degrades cellulose in single cellobiose steps. *Nat. Commun.* **6**, 10149 (2015).
30. A. Griffo *et al.*, Binding forces of cellulose binding modules on cellulosic nanomaterials. *Biomacromolecules* **20**, 769–777 (2019).
31. M. Zhang, S.-C. Wu, W. Zhou, B. Xu, Imaging and measuring single-molecule interaction between a carbohydrate-binding module and natural plant cell wall cellulose. *J. Phys. Chem. B* **116**, 9949–9956 (2012).
32. M. Zhang, B. Wang, B. Xu, Mapping single molecular binding kinetics of carbohydrate-binding module with crystalline cellulose by atomic force microscopy recognition imaging. *J. Phys. Chem. B* **118**, 6714–6720 (2014).
33. J. R. King, C. M. Bowers, E. J. Toone, Specific binding at the cellulose binding module-cellulose interface observed by force spectroscopy. *Langmuir* **31**, 3431–3440 (2015).
34. M. Zhang, B. Wang, B. Xu, Measurements of single molecular affinity interactions between carbohydrate-binding modules and crystalline cellulose fibrils. *Phys. Chem. Chem. Phys.* **15**, 6508–6515 (2013).
35. S. P. S. Chundawat *et al.*, Molecular origins of reduced activity and binding commitment of processive cellulases and associated carbohydrate-binding proteins to cellulose III. *J. Biol. Chem.* **296**, 100431 (2021).
36. G. Sitters *et al.*, Acoustic force spectroscopy. *Nat. Methods* **12**, 47–50 (2015).
37. D. Kamsma, R. Creighton, G. Sitters, G. J. L. Wuite, E. J. G. Peterman, Tuning the music: Acoustic force spectroscopy (AFS) 2.0. *Methods* **105**, 26–33 (2016).
38. F. Ritort, Single-molecule experiments in biological physics: Methods and applications. *J. Phys. Condens. Matter* **18**, R531–R583 (2006).
39. E. Evans, Energy landscapes of biomolecular adhesion and receptor anchoring at interfaces explored with dynamic force spectroscopy. *Faraday Discuss.* **111**, 1–16 (1998).
40. F. Rico, V. T. Moy, Energy landscape roughness of the streptavidin-biotin interaction. *J. Mol. Recognit.* **20**, 495–501 (2007).
41. R. P. Goodman *et al.*, A facile method for reversibly linking a recombinant protein to DNA. *ChemBioChem* **10**, 1551–1557 (2009).
42. G. D. Meredith, H. Y. Wu, N. L. Allbritton, Targeted protein functionalization using His-tags. *Bioconjug. Chem.* **15**, 969–982 (2004).
43. J. Shimada, T. Maruyama, M. Kitaoka, N. Kamiya, M. Goto, DNA-enzyme conjugate with a weak inhibitor that can specifically detect thrombin in a homogeneous medium. *Anal. Biochem.* **414**, 103–108 (2011).
44. J. Shimada *et al.*, Conjugation of DNA with protein using His-tag chemistry and its application to the aptamer-based detection system. *Biotechnol. Lett.* **30**, 2001–2006 (2008).
45. L. Schmitt, M. Ludwig, H. E. Gaub, R. Tampé, A metal-chelating microscopy tip as a new toolbox for single-molecule experiments by atomic force microscopy. *Biophys. J.* **78**, 3275–3285 (2000).
46. C. Verbelen, H. J. Gruber, Y. F. Dufrene, The NTA-His6 bond is strong enough for AFM single-molecular recognition studies. *J. Mol. Recognit.* **20**, 490–494 (2007).
47. F. Kienberger *et al.*, Recognition force spectroscopy studies of the NTA-His6 bond. *Single Mol.* **1**, 59–65 (2000).
48. M. Conti, G. Falini, B. Samorì, How strong is the coordination bond between a histidine tag and Ni-nitritriacetate? An experiment of mechanochemistry on single molecules. *Angew. Chem. Int. Ed. Engl.* **39**, 215–218 (2000).
49. R. W. Friddle, A. Noy, J. J. De Yoreo, Interpreting the widespread nonlinear force spectra of intermolecular bonds. *Proc. Natl. Acad. Sci. U.S.A.* **109**, 13573–13578 (2012).
50. E. D. Cranston, D. G. Gray, Morphological and optical characterization of polyelectrolyte multilayers incorporating nanocrystalline cellulose. *Biomacromolecules* **7**, 2522–2530 (2006).
51. E. Kontturi *et al.*, Cellulose nanocrystal submonolayers by spin coating. *Langmuir* **23**, 9674–9680 (2007).
52. T. Odijk, Stiff chains and filaments under tension. *Macromolecules* **28**, 7016–7018 (1995).
53. D. Freedman, P. Diaconis, On the histogram as a density estimator: L2 theory. *Z. Wahrscheinlichkeitstheor. Verwandte Geb.* **57**, 453–476 (1981).
54. O. K. Dudko, G. Hummer, A. Szabo, Intrinsic rates and activation free energies from single-molecule pulling experiments. *Phys. Rev. Lett.* **96**, 108101 (2006).
55. O. K. Dudko, G. Hummer, A. Szabo, Theory, analysis, and interpretation of single-molecule force spectroscopy experiments. *Proc. Natl. Acad. Sci. U.S.A.* **105**, 15755–15760 (2008).
56. M. R. Nimlos *et al.*, Binding preferences, surface attachment, diffusivity, and orientation of a family 1 carbohydrate-binding module on cellulose. *J. Biol. Chem.* **287**, 20603–20612 (2012).
57. C. Aulin *et al.*, Nanoscale cellulose films with different crystallinities and mesostructures—Their surface properties and interaction with water. *Langmuir* **25**, 7675–7685 (2009).
58. S. Ahola, J. Salimi, L.-S. Johansson, J. Laine, M. Österberg, Model films from native cellulose nanofibrils. Preparation, swelling, and surface interactions. *Biomacromolecules* **9**, 1273–1282 (2008).
59. R. J. Moon, A. Martini, J. Nairn, J. Simonsen, J. Youngblood, Cellulose nanomaterials review: Structure, properties and nanocomposites. *Chem. Soc. Rev.* **40**, 3941–3994 (2011).
60. T. Abitbol, A. Palermo, J. M. Moran-Mirabal, E. D. Cranston, Fluorescent labeling and characterization of cellulose nanocrystals with varying charge contents. *Biomacromolecules* **14**, 3278–3284 (2013).
61. Z. Huang, V. S. Raghuvanshi, G. Garnier, Functionality of immunoglobulin G and immunoglobulin M antibody physisorbed on cellulosic films. *Front. Bioeng. Biotechnol.* **5**, 41 (2017).
62. S. M. Sedlak *et al.*, Direction matters: Monovalent streptavidin/biotin complex under load. *Nano Lett.* **19**, 3415–3421 (2019).
63. S. W. Stahl *et al.*, Single-molecule dissection of the high-affinity cohesin-dockerin complex. *Proc. Natl. Acad. Sci. U.S.A.* **109**, 20431–20436 (2012).
64. B. Alberts, G. Herrick, [11]DNA-cellulose chromatography. *Methods Enzymol.* **21**, 198–217.
65. B. J. Boese, R. R. Breaker, In vitro selection and characterization of cellulose-binding DNA aptamers. *Nucleic Acids Res.* **35**, 6378–6388 (2007).
66. B. Arslan *et al.*, The effects of noncellulosic compounds on the nanoscale interaction forces measured between carbohydrate-binding module and lignocellulosic biomass. *Biomacromolecules* **17**, 1705–1715 (2016).
67. L. Artzi, E. A. Bayer, S. Morais, Cellulosomes: Bacterial nanomachines for dismantling plant polysaccharides. *Nat. Rev. Microbiol.* **15**, 83–95 (2017).
68. T. Verdoerfer *et al.*, Combining in vitro and in silico single-molecule force spectroscopy to characterize and tune cellulosomal scaffoldin mechanics. *J. Am. Chem. Soc.* **139**, 17841–17852 (2017).
69. A. Galera-Prat, S. Morais, Y. Vazana, E. A. Bayer, M. Carrión-Vázquez, The cohesin module is a major determinant of cellulosome mechanical stability. *J. Biol. Chem.* **293**, 7139–7147 (2018).
70. M. A. Jobst *et al.*, Resolving dual binding conformations of cellulosome cohesin-dockerin complexes using single-molecule force spectroscopy. *eLife* **4**, e10319 (2015).
71. Z. Liu *et al.*, High force catch bond mechanism of bacterial adhesion in the human gut. *Nat. Commun.* **11**, 4321 (2020).
72. J. J. Adams *et al.*, Insights into higher-order organization of the cellulosome revealed by a dissect-and-build approach: Crystal structure of interacting *Clostridium thermocellum* multimodular components. *J. Mol. Biol.* **396**, 833–839 (2010).
73. J. M. Moran-Mirabal, J. C. Bolewski, L. P. Walker, Thermobifida fusca cellulases exhibit limited surface diffusion on bacterial micro-crystalline cellulose. *Biotechnol. Bioeng.* **110**, 47–56 (2013).
74. E. J. Jervis, C. A. Haynes, D. G. Kilburn, Surface diffusion of cellulases and their isolated binding domains on cellulose. *J. Biol. Chem.* **272**, 24016–24023 (1997).
75. G. Carrard, A. Koivula, H. Söderlund, P. Béguin, Cellulose-binding domains promote hydrolysis of different sites on crystalline cellulose. *Proc. Natl. Acad. Sci. U.S.A.* **97**, 10342–10347 (2000).
76. J. M. Malho *et al.*, Enhanced plastic deformations of nanofibrillated cellulose film by adsorbed moisture and protein-mediated interactions. *Biomacromolecules* **16**, 311–318 (2015).
77. A. Wierzbza, U. Reichl, R. F. B. Turner, R. A. J. Warren, D. G. Kilburn, Adhesion of mammalian cells to a recombinant attachment factor, CBD/RGD, analyzed by image analysis. *Biotechnol. Bioeng.* **46**, 185–193 (1995).
78. R. S. Reiner, A. W. Rudie, “Process scale-up of cellulose nanocrystal production to 25 kg per batch at the Forest Products Laboratory” in *Production and Applications of Cellulose Nanomaterials*, M. T. Postek, R. J. Moon, A. W. Rudie, M. A. Bilodeau, Eds. (TAPPI Press, 2013), pp. 21–24.
79. T. C. F. Gomes, M. S. Skaf, Cellulose-builder: A toolkit for building crystalline structures of cellulose. *J. Comput. Chem.* **33**, 1338–1346 (2012).
80. M. V. Shapovalov, R. L. Dunbrack Jr., A smoothed backbone-dependent rotamer library for proteins derived from adaptive kernel density estimates and regressions. *Structure* **19**, 844–858 (2011).
81. S. Le Grand, A. W. Götz, R. C. Walker, SPFP: Speed without compromise—A mixed precision model for GPU accelerated molecular dynamics simulations. *Comput. Phys. Commun.* **184**, 374–380 (2013).
82. A. Edelstein, N. Amodaj, K. Hoover, R. Vale, N. Stuurman, Computer control of microscopes using µmanager. *Curr. Protoc. Mol. Biol.* **92**, 1–17 (2010).
83. M. A. Model, J. K. Burkhardt, A standard for calibration and shading correction of a fluorescence microscope. *Cytometry* **44**, 309–316 (2001).
84. M. D. Wang, H. Yin, R. Landick, J. Gelles, S. M. Block, Stretching DNA with optical tweezers. *Biophys. J.* **72**, 1335–1346 (1997).